The Astrophysical Journal, 978:38 (17pp), 2025 January 01 https://doi.org/10.3847/1538-4357/ad9b09
© 2024. The Author(s). Published by the American Astronomical Society.
OPEN ACCESS

Self-interacting Dark Matter, Core Collapse, and the Galaxy–Galaxy Strong-lensing Discrepancy

Isaque Dutra[1], Priyamvada Natarajan[1,2], and Daniel Gilman[3]
[1] Department of Physics, Yale University, New Haven, CT 06511, USA; isaque.dutra@yale.edu
[2] Department of Astronomy, Yale University, New Haven, CT 06511, USA
[3] Department of Astronomy & Astrophysics, University of Chicago, Chicago, IL 60637, USA
Received 2024 June 23; revised 2024 November 13; accepted 2024 December 02; published 2024 December 24

Abstract

Gravitational lensing by galaxy clusters has emerged as a powerful tool to probe the standard cold dark matter (CDM) paradigm of structure formation in the Universe. Despite the remarkable explanatory power of CDM on large scales, tensions with observations on small scales have been reported. Recent studies find that the observational cross section for galaxy–galaxy strong lensing (GGSL) in clusters exceeds the CDM prediction by more than an order of magnitude and persists even after rigorous examination of various possible systematics. We investigate the impact of modifying the internal structure of cluster dark matter subhalos on GGSL and report that altering the inner density profile, given by r^{γ}, to steeper slopes with $\gamma > 2.5$ can alleviate the GGSL discrepancy. This is steeper than slopes obtained with the inclusion of the contribution of baryons to the inner regions of these subhalos. Deviating from the $\gamma \sim 1.0$ cusps that CDM predicts, these steeper slopes could arise in models of self-interacting dark matter undergoing core collapse. Our results motivate additional study of subhalo core collapse in dense cluster environments.

Unified Astronomy Thesaurus concepts: Cosmology (343); Dark matter (353); Galaxy dark matter halos (1880); Strong gravitational lensing (1643); Galaxy clusters (584)

1. Introduction

The concordance cosmological model of cold dark matter (CDM) posits that dark matter behaves as a collisionless fluid and forms gravitationally bound halos with masses $M \sim 10^{14}\ M_{\odot}$ down to structures comparable to Earth mass, $M \sim 10^{-6}\ M_{\odot}$. CDM halos form with an internal density distribution that is well fit by the Navarro–Frenk–White (NFW) profile (J. F. Navarro et al. 1997). Deviation of detected halo properties from these predictions could signal new physics; therefore, many cosmic probes seek to characterize the properties of dark matter halos across a wide range of scales and cosmic environments.

On large cosmological scales, observations agree remarkably well with CDM predictions (D. N. Spergel et al. 2007; Planck Collaboration et al. 2020). However, various tensions have emerged on subgalactic scales, in dark matter halos below masses of $10^{11}\ M_{\odot}$ (see J. S. Bullock & M. Boylan-Kolchin 2017, and references therein). On larger cluster-mass scales of $\sim 10^{14}\ M_{\odot}$, the "arc statistics" tension initially reported by M. Bartelmann et al. (1998) highlighted the inability of CDM simulations to reproduce the abundance of observed lensed arcs, but several plausible resolutions to resolve this discrepancy have since emerged. Despite the variety of observables and cosmic environments associated with the small-scale and cluster-scale tensions, the common theme among them relates to an apparent failure of simulations to simultaneously reproduce the abundance and internal structure of dark matter halos predicted by CDM. Some of these tensions with CDM predictions were interpreted as a serious crisis for the theory and the underlying assumptions related to dark matter physics. In many if not most instances, however, the implications for dark matter physics became less clear upon further investigation of the implementation of baryonic feedback in galaxy formation simulations. These astrophysical processes can alter the properties of dark matter halos without requiring modifications to the fundamental nature of dark matter.[4]

In this paper, we review and revisit the report of an observational probe of small-scale structure, galaxy–galaxy strong lensing (GGSL), that reveals a brand-new tension with predictions of the CDM paradigm (M. Meneghetti et al. 2020, hereafter M20). Comparing lensing observations with the Illustris-TNG cosmological simulation suite, we independently compute the GGSL probability adopting a different methodology from M20 and reaffirm its persistence. We then explore potential explanations to alleviate this discrepancy.

The outline of our paper is as follows. In Section 2, we review the GGSL discrepancy and outline the methodology, including modeling of cluster lenses and the calculation of GGSL from lens mass models in Section 3. The properties of the observed lenses studied here are summarized in Section 4, and the computation of GGSL from the mass-matched simulated analogs from the Illustris-TNG suite is described in Section 5. Alteration of the inner density profile of cluster subhalos explored with the Lenstronomy package is described in Section 6, and the results of our analysis and our conclusions and discussion are presented in Sections 7 and 8, respectively.

2. The GGSL Discrepancy

Gravitational lensing by massive galaxy clusters offers a stringent test of the CDM paradigm of structure formation in terms of both the number of collapsed halos—the subhalo mass

Original content from this work may be used under the terms of the Creative Commons Attribution 4.0 licence. Any further distribution of this work must maintain attribution to the author(s) and the title of the work, journal citation and DOI.

[4] See review by Popolo & Le Delliou (2017; https://hal.archives-ouvertes.fr/hal-01324388v2/document) and references therein.

function—and their density profiles (see the recent review by P. Natarajan et al. 2024). In this work, we focus on the relatively new tension with CDM in galaxy clusters first reported in M20. M20 showed that the measured GGSL cross section of galaxy clusters exceeds the value computed from hydrodynamical CDM simulations. For a fixed total number of cluster subhalos, the GGSL cross section depends principally on the internal structure of the subhalos. More centrally concentrated subhalos are more likely to become supercritical and produce multiple images of background sources. Previously, several works showed that observed clusters contain more high-circular-velocity subhalos (i.e., subhalos with maximum circular velocities $V_{\rm circ} > 100\,{\rm km\,s^{-1}}$) compared to simulations (C. Grillo et al. 2015; E. Munari et al. 2016; M. Bonamigo et al. 2017; M20), although this feature was not quantified in terms of the strong-lensing cross section at that time.

Mirroring the historical progression of apparent tensions with CDM on smaller scales, several studies highlighted possible solutions to the tension reported by M20 based on astrophysics or systematics in the simulations. These include numerical resolution effects (A. Robertson 2021; see also F. C. van den Bosch et al. 2018) or choices related to the implementation of baryonic physics (Y. M. Bahé 2021). Further investigation found that neither of these factors resolves the GGSL tension without creating further new tensions between simulations and observations (M. Meneghetti et al. 2022; A. Ragagnin et al. 2022; Y. M. Tokayer et al. 2024). Resolutions proposed for the other small-scale tensions pertaining to the inner density profiles of low-mass galaxies through baryonic physics effects in fact exacerbate the GGSL tension, which requires an enhancement, not a suppression, of the central density of cluster subhalos.

Despite the significant advances of the past two decades in understanding the interplay between baryonic physics and dark matter physics inside halos (A. Di Cintio et al. 2014a, 2014b; Á. Moliné et al 2017, 2023; F. M. Heinze et al. 2023), as well as the numerical advances in the modeling of these processes in clusters, at present, no clear resolution to the GGSL discrepancy exists within the framework of CDM, as demonstrated in recent work by Y. M. Tokayer et al. (2024) and explored here further.

The investigation by Y. M. Tokayer et al. (2024) examined two key issues. First, they altered the inner density of the pseudo-isothermal profile used to model the dark matter subhalo, which includes a core, produced by `Lenstool` and as employed in the GGSL computation for cluster lens models from M20. These modified profiles were adjusted to fit a truncated NFW (tNFW) profile, ensuring that they remained consistent with observed lensing constraints and adhered to the ΛCDM model. Second, they included the effects of the baryonic component and applied an extreme form of adiabatic contraction to the tNFW profiles,[5] as expected in ΛCDM. Including the modification due to the presence of baryons produced a noticeable effect, and Y. M. Tokayer et al. (2024) showed that it can lead to a steepening of the inner density slope of utmost $\gamma < 2$, where r^{γ} is the inner slope. This is consistent with the results found by F. M. Heinze et al. (2023) when investigating baryonic effects on the inner density slope in the TNG50 simulation. However, even including these modifications, the computed GGSL probability is still significantly discrepant with observations, and these modifications are insufficient to bridge the gap between simulations and lensing observations. In summary, even with adjustments to both the density profile and baryon-driven effects—each designed to stay within the bounds of ΛCDM—the calculated GGSL probability remained significantly discrepant, indicating the persistence of the tension between observations and simulations.

The tension reported by M20 implies that the concentration of matter in the inner regions of cluster subhalos significantly exceeds the CDM prediction. As they note, this implies either missing physics in the simulations that would increase the cluster subhalo lensing efficiency or a modification to the internal structure of the subhalos that raises their strong-lensing cross section. In this paper, we investigate the GGSL under the assumption that modifications to the internal structure of cluster subhalos are required to resolve the tension.

3. Methodology

3.1. Modeling Cluster Lenses

We briefly outline the standard procedures used to model observed cluster lenses using parametric mass profiles that are apt and amenable for direct and easy comparison with simulated mass-matched cluster analogs. More details of this procedure can be found in the review by J.-P. Kneib & P. Natarajan (2011).

1. The total mass distribution of a galaxy cluster is decomposed into a parametric mass profile with components to represent larger-scale and smaller-scale contributions (P. Natarajan & J.-P. Kneib 1997):

$$\phi_{\rm tot} = \sum_i \phi_i^{\rm halo} + \sum_j \phi_j^{\rm sub} + \phi_{\kappa,\gamma}, \quad (1)$$

where the first term represents large-scale smooth halos associated with the overall cluster potential on scales of hundreds of kiloparsecs, the second term represents smaller-scale perturbations on kiloparsec scales that are associated with the subhalos of cluster member galaxies, and the last term is associated with a possible constant convergence or shear field, referred to as the mass-sheet degeneracy. Observed strong- and weak-lensing constraints, including the positions, brightnesses, and shapes of lensed background galaxies, are used to constrain the overall mass distribution represented by Equation (1). It has been shown that measurements of the shear and convergence for extremely well-calibrated lensing clusters with multiple families of strongly lensed images with spectroscopic redshifts such as the ones studied here can be used to determine the mass-sheet degeneracy term above (M. Bradač et al. 2004; M. Rexroth et al. 2016; P. Bergamini et al. 2021). The components in Equation (1) are determined using lens inversion algorithms, for instance, the publicly available software package `Lenstool` that is widely used by the lensing community including M20 and `lenstronomy`, a new package that we use for the analysis presented here. Both the larger-scale halos and subhalos are parameterized by self-similar dual pseudo-isothermal elliptical mass distributions (dPIE profiles) in `Lenstool` (Á. Elìasdóttir

[5] By using the publicly available code `Contra` found at https://websites.umich.edu/~ognedin/contra/.

et al 2007):

$$\rho_{\rm dPIE}(r) = \frac{\rho_0}{(1 + r^2/r_{\rm core}^2)(1 + r^2/r_{\rm cut}^2)}. \quad (2)$$

2. The enclosed projected total mass can be found with

$$M_{\rm 2D}(R) = 2\pi\Sigma_0 \frac{r_{\rm core} r_{\rm cut}}{r_{\rm cut} - r_{\rm core}} (\sqrt{r_{\rm core}^2 + R^2} - r_{\rm core} - \sqrt{r_{\rm cut}^2 + R^2} + r_{\rm cut}), \quad (3)$$

3. where the projected surface mass density $\Sigma(R)$ is given by

$$\Sigma(R) = \Sigma_0 \frac{r_{\rm core} r_{\rm cut}}{r_{\rm cut} - r_{\rm core}} \left(\frac{1}{\sqrt{r_{\rm core}^2 + R^2}} - \frac{1}{\sqrt{r_{\rm cut}^2 + R^2}} \right), \quad (4)$$

4. and ρ_0 and Σ_0 can be related to the fiducial velocity dispersion from

$$\sigma_{\rm dPIE}^2 = \frac{4}{3} G\pi\rho_0 \frac{r_{\rm core}^2 r_{\rm cut}^3}{(r_{\rm cut} - r_{\rm core})(r_{\rm cut} + r_{\rm core})^2} \quad (5)$$

$$= \frac{4}{3} G\Sigma_0 \frac{r_{\rm core} r_{\rm cut}^2}{r_{\rm cut}^2 - r_{\rm core}^2}, \quad (6)$$

where $\sigma_{\rm dPIE}$ is found from the lens model optimization obtained by reproducing observed lensed image constraints and is related to the measured central velocity dispersion of cluster galaxies via $\sigma_{\rm dPIE}^2 = \frac{2}{3}\sigma_0^2$. The following substitution is done to generalize to the elliptical case, $R \rightarrow \tilde{R}$, profiles that are available for use within `Lenstool`:

$$\tilde{R}^2 = \frac{X^2}{(1 + \epsilon)^2} + \frac{Y^2}{(1 - \epsilon)^2}, \quad (7)$$

where the ellipticity $\epsilon = (A - B)/(A + B)$, where A and B are the semimajor and semiminor axis, respectively. The ellipticity as defined in `Lenstool` has a slightly different definition as $\hat{\epsilon}$ that is given by

$$\hat{\epsilon} = \frac{A^2 - B^2}{A^2 + B^2}. \quad (8)$$

The dPIE profiles in `Lenstool` are parameterized by projected sky positions x and y, fiducial velocity dispersion $\sigma_{\rm dPIE}$, ellipticity $\hat{\epsilon}$, scale radius $r_{\rm core}$, cut radius $r_{\rm cut}$, and orientation $\theta_{\hat{\epsilon}}$. The best-fit cluster lensing model provides constraints on the total mass enclosed within $r_{\rm cut}$ of the larger-scale halos as well as the integrated mass within $r_{\rm cut}$ for the subhalos. How the mass and surface mass density are distributed radially within subhalos is not a quantity that can be currently constrained with the data in hand. Furthermore, to even obtain this integrated constraint on the mass enclosed within the aperture for subhalos, we need to collapse the number of parameters required to describe galaxy-scale subhalos and the associated cluster member galaxies. To do this, typically, an explicit relation between mass and light that is empirically well motivated for cluster galaxies is assumed. The following scaling relations with luminosity L are adopted involving the characteristic subhalo parameters ($\sigma_{\rm dPIE}$, $r_{\rm cut}$) (see Á. Elìasdóttir et al 2007):

$$\sigma_{\rm dPIE} = \sigma_{\rm dPIE}^{\rm ref} \left(\frac{L}{L_*} \right)^{\alpha}, \quad (9)$$

$$r_{\rm cut} = r_{\rm cut}^{\rm ref} \left(\frac{L}{L_*} \right)^{\beta}. \quad (10)$$

Therefore, for a well-constrained lens model, masses are obtained for all constituent subhalos using the above calibrated scaling relation; with these, the overall subhalo mass function can be determined for a given cluster.

3.2. Calculation of the GGSL

In this section, we briefly define the GGSL probability and outline its calculation. Starting from the surface mass density maps of the lensing clusters obtained as noted above, we are interested in computing the probability that a background source could be strongly lensed by foreground substructures, namely, subhalos in the cluster.

All lensing quantities of interest can be derived from the projected Newtonian potential ϕ related to the projected surface mass density Σ as $4\pi G\Sigma = \nabla^2\phi$. These can be directly obtained from the derived lensing mass maps. The deflection angle α is found from the partial derivative of the projected potential, while computed second-order derivatives characterize induced deformations: the convergence κ quantifies the isotropic deformation and affects the apparent size and brightness of the lensed objects, while the shear γ describes the anisotropic deformation affecting the stretching along the shear direction. The convergence κ and shear γ define the magnification $\mu^{-1} = (1 - \kappa)^2 - \gamma^2 = (1 - \kappa - \gamma)(1 - \kappa + \gamma)$, which is infinite when $\kappa \pm \gamma = 1$. The set of points of infinite magnification in the image plane define two closed lines, the *critical lines*, with *caustics* being the corresponding lines projected onto the source plane. For a simple mass distribution, the inner critical line can be identified as the *radial* critical line, where background sources are deformed radially, and the outer one as the *tangential* critical line, where background sources are tangentially deformed into arcs and rings. Since the radial critical lines of massive cluster members are expected to be insignificant in terms of area enclosed within (see M20, supplementary materials), we consider only the tangential critical lines where $\kappa + \gamma = 1$. We plot the tangential critical lines and caustics for one of the clusters studied here, MACS J1206, in Figure 1.

Critical lines can be assigned an Einstein radius $\theta_{\rm E}$ given their average enclosed area A, $\theta_{\rm E} = \sqrt{A/\pi}$. Following the same classification criteria adopted in M. Meneghetti et al. (2022), we identify critical lines with $\theta_{\rm E} > 5''$ as *primary* and those with $0\farcs5 < \theta_{\rm E} < 3''$ as *secondary* and exclude the rest in our analysis. We adopt the same definitions as M20 for

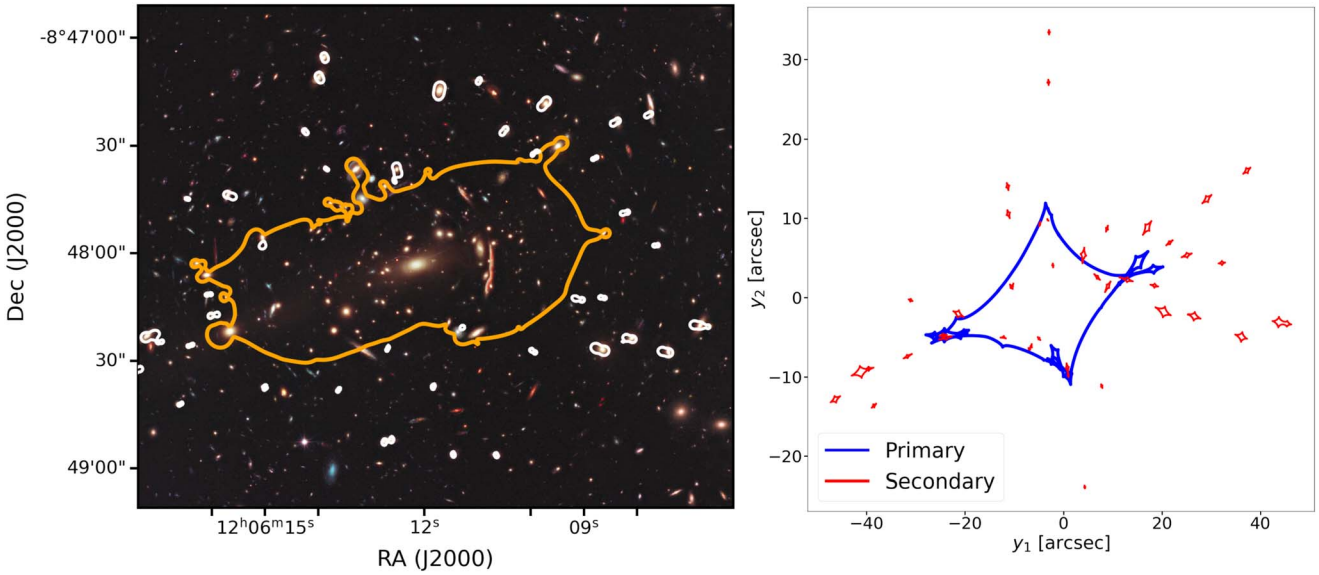

Figure 1. The critical lines and caustics for the cluster MACS J1206 calculated using `lenstronomy`; these are shown in the left and right panels, respectively. The primary critical line is identified in orange, while secondaries are shown in white; similarly, primary caustics are identified in blue, while secondary caustics are shown in red. Image credit: the color composite of MACS J1206, NASA, ESA, M. Postman (STScI) and the CLASH Team. We note here that the FOV in the left panel is not the same as the FOV in the right panel. The caustics are smaller and harder to see; therefore, we present a zoomed-in view in the right panel for visibility.

consistency for comparison. These selection criteria permit us to filter subhalos with masses in the range of $\sim 10^{10-12}\, h^{-1}\, M_{\odot}$. And by definition, GGSL events originate from the secondary critical lines associated with cluster subhalos in this mass range. Substructure associated with Einstein radii less than $0\farcs5$ cannot be resolved by simulations, while those with Einstein radii ranging between $3''$ and $5''$ are associated with larger, group-scale masses and not individual galaxies (M. Meneghetti et al. 2022, 2023; A. Ragagnin et al. 2022). The GGSL cross section $\sigma_{\rm GGSL}$ is defined as the total area enclosed by all secondary caustics. Since both the convergence κ and shear γ depend on the source redshift z, $\sigma_{\rm GGSL} = \sigma_{\rm GGSL}(z)$ is also a function of redshift. The probability of GGSL events $P_{\rm GGSL}$ is defined as the GGSL cross section normalized by the field-of-view (FOV) area on the source plane $A_{\rm s}$, $P_{\rm GGSL} = \sigma_{\rm GGSL}/A_{\rm s}$.

In summary, the caustics associated with subhalos mark regions where background galaxies will be strongly lensed and dividing the caustic area by the FOV source plane area defines the probability of GGSL events. It is this derived probability that M20 found to be higher by more than an order of magnitude for observed lensing clusters compared to their simulated counterparts in ΛCDM.

Here, we adopt a new approach and utilize the recently developed open-source gravitational-lensing python package `lenstronomy` (S. Birrer & A. Amara 2018; S. Birrer et al. 2021) to perform the lensing calculations. For each cluster, we first load the list of best-fit potentials and their optimized characteristic properties obtained from `Lenstool` representing all cluster members and initialize the appropriate analytical potentials in `lenstronomy`. For a given source redshift, the deflection map and its relevant derivatives are calculated, as are the maps for the convergence κ and shear γ. The contours where $\kappa + \gamma = 1$ are found utilizing the open-source package `scikit-image` (Van Der Walt 2014), and by projecting them onto the source plane, the associated caustics are found. Consistent with M20, we delimit the FOV to $200'' \times 200''$ for all the clusters studied here. Then the areas associated with secondary caustics are summed and normalized by the projected FOV area to compute the $P_{\rm GGSL}(z_s)$ for source redshifts z_s between 0.5 and 7.

We calculate the properties of cluster subhalos required to reproduce the observed GGSL cross section. This work expands on the earlier analysis by D. Yang & H.-B. Yu (2021), who showed that core collapse in self-interacting dark matter (SIDM) models raises the central density of cluster subhalos and can hence increase the GGSL cross section. Here, we explore more comprehensively the consequence of core collapse by calculating the strong-lensing cross section with the convergence maps of simulated galaxy clusters. To examine the degree to which feedback processes can impact the computed GGSL, we analyze a new simulation suite—the Illustris-TNG suite[6]—for comparison with lensing data that implements feedback differently from the DIANOGA suite used for comparison by M20. Unlike in DIANOGA, in the Illustris suite of simulations, feedback from star formation and accreting black holes is modeled very differently. Stellar feedback is driven by galactic-scale outflows, and multimodal feedback from accreting black holes that operate in a thermal quasar mode at high accretion rates and a kinetic wind mode at low accretion rates inform their subgrid feedback physics models. These implementations of feedback are calibrated to quench the gas cooling and star formation that is required to match the properties of observed galaxies. These astrophysical processes are relevant to GGSL, as they potentially serve to rearrange mass from the inner regions of halos.

In what follows, we compute the GGSL cross section for a sample of simulated clusters that are matched in total mass enclosed within R_{200}[7] to a set of observed lenses (see Table 1 for the list). We calculate the GGSL from simulated clusters using the software package *lenstronomy*[8] (S. Birrer &

[6] More information on the TNG suite can be found at https://www.tng-project.org/.

[7] Where R_{200} is the radius within which the density is 200 times the critical density of the Universe at the halo's redshift z.

[8] https://github.com/lenstronomy/lenstronomy

Table 1
Summary of the Observed Cluster Lenses in Our Sample

Cluster	Redshift	M_{200} Estimate ($10^{15}\ M_{\odot}$)	Subhalos
Abell 2744	0.308	$2.22\ ^{+0.13}_{-0.12}$	246
Abell S1063	0.348	$3.97\ ^{+1.6}_{-0.9}$	222
MACS J0416	0.397	1.60 ± 0.01	191
MACS J1206	0.439	1.4 ± 0.2	258
PSZ1 G311	0.444	0.85	194

A. Amara 2018; S. Birrer et al. 2021), a different code than the `Lenstool` software used by M20.[9] Using `lenstronomy`, we modify the properties of Illustris-TNG CDM cluster subhalo density profiles to more centrally concentrated density profiles. In particular, we consider a density profile given by J. A. Munoz et al. (2001),

$$\rho_{\rm gNFW}(r) = \frac{\rho_0}{(r/r_{\rm s})^{\gamma}(1 + (r/r_{\rm s})^2)^{(\beta-\gamma)/2}} \tag{11}$$

(hereafter the generalized NFW, or gNFW, profile), where γ and β are the logarithmic inner and outer slopes, respectively. An NFW profile in CDM corresponds to $\gamma = 1$ and $\beta = 3$.[10]

To derive the values of γ and β in the density profile given in Equation (11) that are required to match the observed GGSL, we take three separate projections of a simulated galaxy cluster analog and replace cluster subhalos with objects possessing gNFW density profiles. This is implemented in such a way as to conserve the total mass of the cluster while redistributing the mass inside the subhalo. We then compute the GGSL probability with these steepened subhalo profiles.

In addition to calculation of the GGSL outlined above that was performed as done previously by M20 for comparison, in this work, we compute the GGSL probability directly from the particle data in the TNG300 simulation. First, we compute using dark matter particles that include the adiabatic contraction from the baryonic component, and then we explicitly include the dark matter and baryonic particles to compute the GGSL. We find very good agreement with the prior calculation done with NFW profile fits for the simulated clusters. Further details are provided in Appendix C.

4. Properties of the Observed Cluster Lens Sample

With the intention of independently verifying the GGSL probability discrepancy reported by M20, we select five observed cluster lenses to study as our sample. Four of them have well-constrained mass distributions (lensing mass models) derived from the Hubble Frontier Fields (HFF) program data. These four were also selected by M20 and are Abell 2744 (A2744) at $z = 0.308$ (J. Merten et al. 2011; Iu. Babyk et al. 2012; M. Jauzac et al. 2016), Abell S1063 (AS1063) at $z = 0.348$ (P. L. Gómez et al. 2012; D. Gruen et al. 2013), MACS J1206.2–0847 (M1206) at $z = 0.439$ (K. Umetsu et al. 2012; A. Biviano et al. 2013), and MACS J0416.1–2403 (M0416) at $z = 0.397$ (M. Jauzac et al. 2014).

The mass models for these four HFF clusters computed using `Lenstool` are publicly available on MAST.[11] Several groups using independently developed lens inversion algorithms provided magnification and mass maps for the HFF clusters. For our work here, we used the mass models provided by the CATS collaboration. Further details of the `Lenstool` reconstructions from the CATS collaboration can be found in several papers, including but not limited to M. Jauzac et al. (2015, 2016), G. Mahler et al. (2018), P. Bergamini et al. (2019, 2021), and M. Meneghetti et al. (2022). The fifth cluster in our sample, PSZ1 G311.65–18.48 (PG311), also included as part of the sample in M. Meneghetti et al. (2022), is a massive cluster that was selected differently. It was selected not for its lensing properties but from the ESA Planck catalog of clusters that produce a detectable Sunyaev–Zel'dovich (SZ) decrement signal (Planck Collaboration et al. 2014). The properties of our selected cluster sample are summarized in Table 1.

A2744 (also known as AC118 or RXC J0014.3–3022) at $z \sim 0.308$ is an exceedingly complex system undergoing a complicated merging event and has been dubbed Pandora's Cluster. It displays a total of about 34 strongly lensed images identified in 11 multiple-image systems (J. Merten et al. 2011) and was chosen for the HFF by J. M. Lotz et al. (2017) and, more recently, also observed as part of the JWST UNCOVER program (R. Bezanson et al. 2024). The total enclosed mass within a radius of 1.3 Mpc for A2744 was measured to be $(1.8 \pm 0.4) \times 10^{15}\ M_{\odot}$ by J. Merten et al. (2011) pre-HFF; and with HFF data, M. Jauzac et al. (2015) measure the total cluster mass within 250 kpc as $(2.765 \pm 0.008) \times 10^{14}\ M_{\odot}$ and enclosed within 1.3 Mpc as $(2.3 \pm 0.1) \times 10^{15}\ M_{\odot}$ using strong- and weak-lensing analysis in M. Jauzac et al. (2016). Here, we use the mass estimate of $M_{200} = 2.22^{+0.13}_{-0.12} \times 10^{15} M_{\odot}$ within $R_{200} = 2.38^{+0.36}_{-0.31}$ Mpc. The best-fit lensing model for this cluster comprises 258 total mass components, of which six are large-scale mass concentrations; six are large-scale potentials that lie outside the Hubble Advanced Camera for Surveys FOV but are in the vicinity and need to be included, and the rest correspond to confirmed cluster member galaxies.

AS1063 at $z \sim 0.348$ is a particularly interesting cluster due to its unusually high X-ray luminosity that indicates that it recently underwent a major merging event (P. L. Gómez et al. 2012). Part of the HFF, it was also observed previously by the Hubble Space Telescope (HST) in the Cluster Lensing And Supernova survey with Hubble (CLASH) program (M. Postman et al. 2012) and spectroscopically followed up by the CLASH Very Large Telescope (VLT) program (G. B. Caminha et al. 2016). The estimated mass is $M_{200} = 3.31^{+0.96}_{-0.68} \times 10^{15} M_{\odot}$ (R. Williamson et al. 2011; P. L. Gómez et al. 2012; D. Gruen et al. 2013; J. M. Diego et al. 2016). The best-fit lensing mass model for AS1063 comprises 227 total mass components, of which two represent large-scale central mass concentrations and the rest are all associated with confirmed cluster member galaxies.

M0416 at $z \sim 0.397$ is also a massive cluster in a complex dynamical state: it features a bimodal velocity distribution showing two central peaks and elongated subclusters suggesting that they are being observed in a precollisional but strongly interacting phase (I. Balestra et al. 2016). It was also imaged by the HFF and CLASH programs and followed up as part of the CLASH-VLT program. Its total projected mass inside a

[9] https://projets.lam.fr/projects/lenstool/wiki

[10] The density profile in Equation (11) differs from an NFW profile through the $(1 + (r/r_{\rm s})^2)$ in the denominator, whereas the NFW profile has $(1 + (r/r_{\rm s}))^2$. This detail, however, is not relevant to our main results.

[11] http://archive.stsci.edu

200 kpc aperture was estimated to be $(1.60 \pm 0.01) \times 10^{14}\ M_{\odot}$ by M. Jauzac et al. (2014), while the CLASH analysis by K. Umetsu et al. (2016) estimates $M_{200} = (1.412 \pm 0.366) \times 10^{15}$, and I. Balestra et al. (2016) report $M_{200} = (1.12 \pm 0.26) \times 10^{15}\ M_{\odot}$ using CLASH-VLT. The best-fit lensing mass model for this cluster contains 197 total mass components, of which six are large-scale central mass concentrations and the rest are associated with confirmed cluster member galaxies.

M1206 at $z \sim 0.440$ was previously studied by H. Ebeling et al. (2009). The CLASH analysis by K. Umetsu et al. (2016) estimates the cluster mass to be $M_{200} = (2.596 \pm 0.604) \times 10^{15}\ M_{\odot}$. The obtained best-fit lensing mass model contains 264 total mass components, of which three are large-scale central potentials; an additional component of external shear and the rest are associated with confirmed cluster member galaxies.

The final selected cluster in our sample is PG311, $z \sim 0.443$. Our current sample has some overlap with the sample analyzed in M20 but also includes PG311, which is not selected via strong lensing, as noted above, but detected in the ESA Planck catalog of SZ sources (Planck Collaboration et al. 2014). It features a remarkable tangential arc, the highly distorted image of a distant star-forming galaxy at $z \sim 2.370$ lensed 12 times, dubbed the *Sunburst Arc* by T. E. Rivera-Thorsen et al. (2017). K. Sharon et al. (2022) estimate the projected cluster mass within 250 kpc to be $2.93^{+0.01}_{-0.02} \times 10^{14} M_{\odot}$ using HST imaging, archival VLT/MUSE spectroscopy, and Chandra X-ray data, while H. Dahle et al. (2016) estimate its mass using Planck SZ data to be $M_{500} = 6.6^{+0.9}_{-1.0} \times 10^{14} M_{\odot}$. Converting to M_{200} using a typical concentration–mass relation, M. Meneghetti et al. (2022) estimated $M_{200} \sim 8.5 \times 10^{14}\ M_{\odot}$. The best-fit lensing mass model contains 202 total mass components, of which eight are large-scale central potentials and the rest are associated with confirmed cluster member galaxies.

We note that our selected sample of clusters is very similar to the one selected by M. Meneghetti et al. (2022) and identical to the clusters selected by Y. M. Tokayer et al. (2024). However, using the best-fit list of mass components from the optimized lensing mass model, here we use both `Lenstool` and `lenstronomy` to calculate the GGSL probability for each of these clusters, as outlined in Section 3.2.

5. Computing GGSL from Mass-matched Simulated Analogs in Illustris-TNG

We calculate the GGSL probability of subhalos in cluster-scale halos in the Illustris-TNG simulations by modeling them with analytical mass density profiles. The Illustris-TNG simulations are a suite of cosmological magnetohydrodynamical simulations of galaxy formation (D. Nelson et al. 2019).[12] In this study, we focus on TNG300, with a periodic box with a side length of 302.6 Mpc, a particle/cell number of 2500^3 for baryons and dark matter, a baryonic particle mass of $1.1 \times 10^7\ M_{\odot}$, and a dark matter particle mass of $5.9 \times 10^7\ M_{\odot}$.

For each cluster in our observational sample, we identify the three best total mass-matched halo analogs in TNG300 with comparable M_{200}s at the same redshift as the observed sample. For the TNG300 cluster halos, M_{200} is estimated using the friends-of-friends algorithm. Our simulated analogs have a mean mass of $\sim 10^{15}\ M_{\odot}$.

[12] Publicly available at https://www.tng-project.org.

We model the central halo and subhalos of the selected TNG300 analogs with the NFW profile, which has been shown to be a good fit for dark matter halos over a wide range of halo masses (J. F. Navarro et al. 1997). It is particularly useful since the profile can be specified with two parameters, which can be chosen to be the radius R_{200}, which encloses an average density of $200\rho_c$, and the scale radius R_s, where the profile's logarithmic slope steepens from -1 to -3.

The density profile is given by

$$\rho_{\rm NFW}(r) = \frac{\delta_c \rho_c}{(r/r_s)(1 + r/r_s)^2}, \tag{12}$$

where $\rho_c \equiv 3H^2(z)/(8\pi G)$ is the critical density of the Universe at the halo's redshift z and δ_c is the characteristic overdensity of the halo, defined as

$$\delta_c \equiv \frac{200}{3} \frac{c^3}{\ln(1 + c) - c/(1 + c)}, \tag{13}$$

where c is the characteristic concentration of the halo, defined as $c \equiv R_{200}/R_s$.

We adopt the same procedure to calculate the GGSL probability for the simulated analogs as done for observed clusters described in Section 4. For each subhalo belonging to the same TNG300 group, we now initialize an NFW profile in `lenstronomy` with the halo's parameters M_{200} and concentration c, wherein the scale radius R_s is found from the relationship $R_{\rm max} \simeq 2.163 R_s$ (H. Mo et al. 2010, Section 11.1.2) and $R_{\rm max}$ is the radius at which the halo's particles attain maximum velocity.

Furthermore, we project each simulated cluster analog and its subhalos along three independent lines of sight corresponding to the simulation's three spatially orthogonal planes to average over. We assume $M_{200} \approx M_{\rm sub}$, the total mass of all bound member particles. We include only subhalos with virial mass M_{200} between $10^{10}\ h^{-1}\ M_{\odot}$ and $10^{12}\ h^{-1}\ M_{\odot}$, as done in M20, in addition to the massive central large-scale halos. Our results confirm the reported tension with CDM, clearly demonstrating the order-of-magnitude gap.

As noted above, we also compute the GGSL for the simulated analogs to our observational sample using the particle data (rather than the halo catalogs) directly and find that the GGSL discrepancy remains. For each matched simulated analog, we projected the smoothed particle data as described in Appendix C and computed the GGSL probability for two distinct cases: (i) dark-matter-only particles from the TNG300-1 simulation that includes baryons in an effort to capture the effect of baryonic-induced adiabatic contraction of the dark matter halos, and (ii) explicitly including both the dark matter and baryonic particles from the TNG300-1 simulation. The resulting GGSL probabilities are shown in Figure 2. The computed caustic maps for the above cases are provided in Appendix C. Furthermore, we also examined the three orthogonal projections for each analog, including the projection along the direction of elongation, and find the difference in GGSL probabilities to be negligible.

6. Altering Inner Density Profiles to Alleviate the GGSL Discrepancy

While baryonic physics can, in principle, impact the central density profiles of halos (A. Di Cintio et al. 2014a, 2014b; Á. Moliné et al 2017, 2023; F. M. Heinze et al. 2023), the

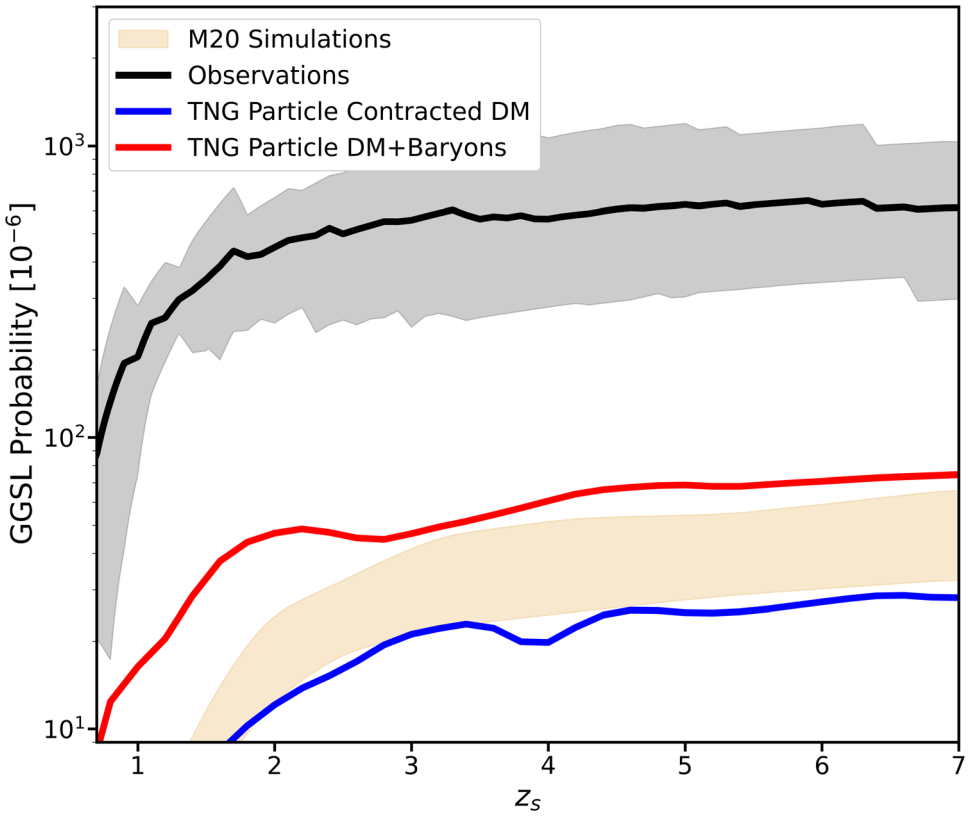

Figure 2. The GGSL probability as a function of source redshift computed by smoothing the particle data from the TNG300 simulations for observed clusters and their mass-matched simulated analogs. The blue curve is the GGSL computed from the analogs taken from the TNG300 with dark matter particles that includes the effects of the induced adiabatic contraction due to the baryons, and in red, we show the GGSL calculated explicitly including all the components—the dark matter, gas, stars, and black holes in the TNG300 simulated cluster analogs.

structure of a dark matter halo can evolve more dramatically if one relaxes the assumption of collisionless dynamics inherent to CDM. The class of theories with this attribute is commonly referred to as SIDM. Dark matter self-interactions were initially proposed as a mechanism to generate flat cores inside halos to explain the low central densities (relative to CDM predictions) of low-mass dwarf galaxies (D. N. Spergel & P. J. Steinhardt 2000). Soon after the initial SIDM proposal, S. Balberg et al. (2002) pointed out that these dark self-interactions could also result in an opposite effect due to the "gravothermal catastrophe," a phenomenon initially studied by D. Lynden-Bell et al. (1968) in the context of dense star clusters. The gravothermal catastrophe, or "core collapse" as it is now more commonly phrased, refers to a runaway contraction of halo density profiles. Core collapse represents the ultimate fate of all halos in SIDM unless an external heat reservoir supplies the central core with sufficient energy to remain intact (e.g., Z. C. Zeng et al. 2022; O. Slone et al. 2023). SIDM models have gained traction on small scales because the processes of core formation and eventual core collapse give rise to a diversity of density profile slopes in subhalos that appears more consistent with the properties of low-mass galaxies (J. Zavala et al. 2019; L. V. Sales et al. 2022; S. Yang et al. 2023).

The process of core collapse is particularly relevant for lensing because core collapse raises the central density, and therefore the lensing efficiency, of a halo. Recently, Q. Minor et al. (2021) reported the detection of a dark object with a central density orders of magnitude higher than the CDM expectation, which could result from core collapse in an SIDM halo (E. O. Nadler et al. 2023). Core collapse can also produce a distinct signal in the magnifications among images of quadruply imaged quasars (D. Gilman et al. 2021, 2023). These studies focus on strong lensing by isolated individual galaxy-scale lenses, unlike the case of GGSL in clusters. Cosmological simulations of SIDM on cluster scales that permit direct comparison and calculation of the GGSL probability are currently unavailable, as there are multiple numerical challenges with resolution and convergence that are yet to be surmounted (e.g., M. S. Fischer et al. 2024; C. Mace et al. 2024; A. Ragagnin et al. 2024).

6.1. Mimicking Core Collapse within Lenstronomy

It is clear that more centrally concentrated subhalos likely enhance GGSL and could therefore alleviate the GGSL discrepancy. This, however, requires steepening the inner density profiles in subhalos beyond $\rho \propto r^{-1}$ of the NFW profile characteristic of CDM. Cluster galaxies are observed to have a strong concentration of baryons in the inner regions; however, as recently shown by Y. M. Tokayer et al. (2024), the modification to the inner density profiles from these effects cannot account for the GGSL discrepancy. In Y. M. Tokayer et al. (2024), the density profiles of cluster galaxies were adjusted to account for extreme baryon-driven adiabatic contraction while still remaining consistent with ΛCDM. However, the resulting change in computed GGSL probability was insufficient to resolve the observed discrepancy.

Such additional steepening is expected to occur in beyond-CDM dark matter models that contain self-interactions, SIDM models. The class of SIDM models in which appreciable

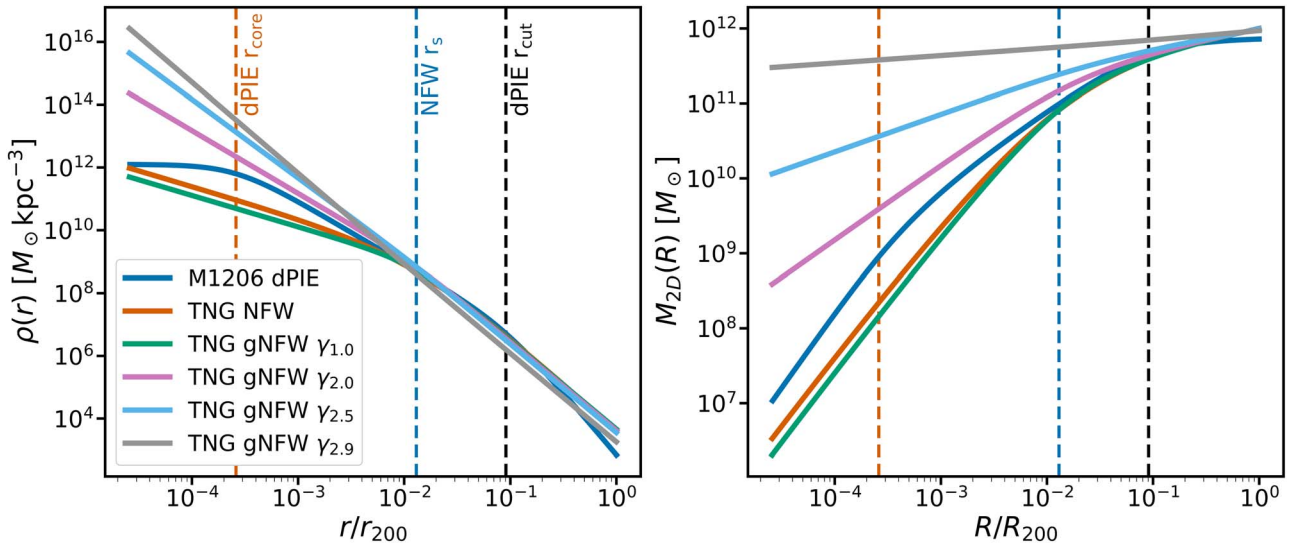

Figure 3. Changes in inner density slope. We show the changes in the density profile shape and the corresponding change in the enclosed projected mass (2D mass) of a fiducial cluster subhalo in the observed lensing cluster M1206 (which is part of our sample) and a subhalo with matching M_{200} from the simulated cluster analog. Note that steepening the inner logarithmic slope γ from 1 to 2.9 results in an enhancement of the central density of the subhalo by 4 orders of magnitude within 0.1 r_{200}.

steepening occurs are ones in which gravothermal core collapse has commenced in the innermost regions. In order to mimic this process of core collapse that results in a more centrally concentrated halo, we utilize the gNFW profile and alter the inner and outer slopes of the mass density profile for simulated subhalos in the simulated analogs. The larger-scale central, smooth halo mass density profiles are kept unaltered and are retained with an NFW fit, as they account for the well-constrained large-scale lensing features in the observed clusters.

We choose the gNFW profile (J. A. Munoz et al. 2001) that is implemented in `lenstronomy` to steepen inner density profiles,

$$\rho_{\rm gNFW}(r) = \frac{\rho_0}{(r/r_{\rm s})^{\gamma}(1+(r/r_{\rm s})^2)^{(\beta-\gamma)/2}}, \tag{14}$$

where γ and β are the logarithmic inner and outer slope, respectively. Compared to standard cusped models such as the NFW profile, where the 3D density profile $\rho \propto (r+r_{\rm s})^{(\beta-\gamma)}$, the gNFW profile implemented in `lenstronomy` follows $\rho \propto (r^2+r_{\rm s}^2)^{(\beta-\gamma)/2}$ and possesses convenient analytic properties that facilitate lensing calculations (J. A. Munoz et al. 2001).

After loading all TNG300 subhalos into `lenstronomy` as described in the previous section for each observed cluster analog, we modify the mass density profile from the CDM NFW profile into a gNFW profile for the subhalo population while conserving mass within R_{200}. This `lenstronomy` profile conversion procedure is done through the open-source python package `pyHalo`.[13] We start by calibrating the gNFW profile by setting $\gamma = 1$ and finding the logarithmic outer slope β such that the caustic area of the subhalo matches the caustic area produced by an NFW profile; this, we find, is the case when $\beta = 2.84$. The outer slope is now fixed to this value, and then we alter the inner slope γ, which mimics various stages of core collapse in generic SIDM models. Next, we recalculate the GGSL probability for each simulated cluster analog by fitting a gNFW profile varying $\gamma = 1.0$, 2.0, 2.5, 2.9, and 2.99 for the entire subhalo population as a whole. All the subhalos in the simulated analog cluster are assigned the same steepened inner slope. The core-collapse cases with $\gamma = 2.5$ and 2.9 are shown in Figure 3 and Figure 4.

The difference in the computed critical lines of a TNG300 cluster analog fitted with an NFW profile and the gNFW with $\gamma = 2.9$ can be seen in Figure 5. As seen, the secondary critical lines for the gNFW profiles representing the core-collapsed subhalos are significantly larger and better resemble the critical lines of observed clusters (see, for example, the case of MACS J1206 shown in Figure 1). We also calculate the GGSL probability for the final stage of gravothermal core collapse to a point mass, as this represents the limiting case. In `lenstronomy`, this case is initialized by specifying the Einstein radius $\theta_{\rm E}$ of the point mass with mass M,

$$\theta_{\rm E}^2 = \frac{4GM}{c^2}\frac{D_{\rm LS}}{D_{\rm S}D_{\rm L}}, \tag{15}$$

where $D_{\rm LS}$ is the angular diameter distance between the lens and source plane, $D_{\rm L}$ is between the observer and the lens plane, and $D_{\rm S}$ is between the observer and the source plane. The GGSL probability of the core-collapse cases c1-SIDM and c2-SIDM and that of the point mass are plotted in Figure 4. For reference, the critical lines and caustics computed from the projected smoothed particle data of the same analogs are shown in Appendix C.

7. Results

We compare lensing observations with a new set of cosmological simulations, TNG300 from the Illustris suite, and compute GGSL using a new modeling procedure, distinct from M20, to verify that the tension persists independently of simulations and modeling assumptions. We find that the GGSL discrepancy persists for cluster lenses, even with our use of a new sample of mass-matched simulated clusters from the TNG300 simulation suite and computation performed using an independent method utilizing the `lenstronomy` software

[13] Publicly available at https://github.com/dangilman/pyHalo.

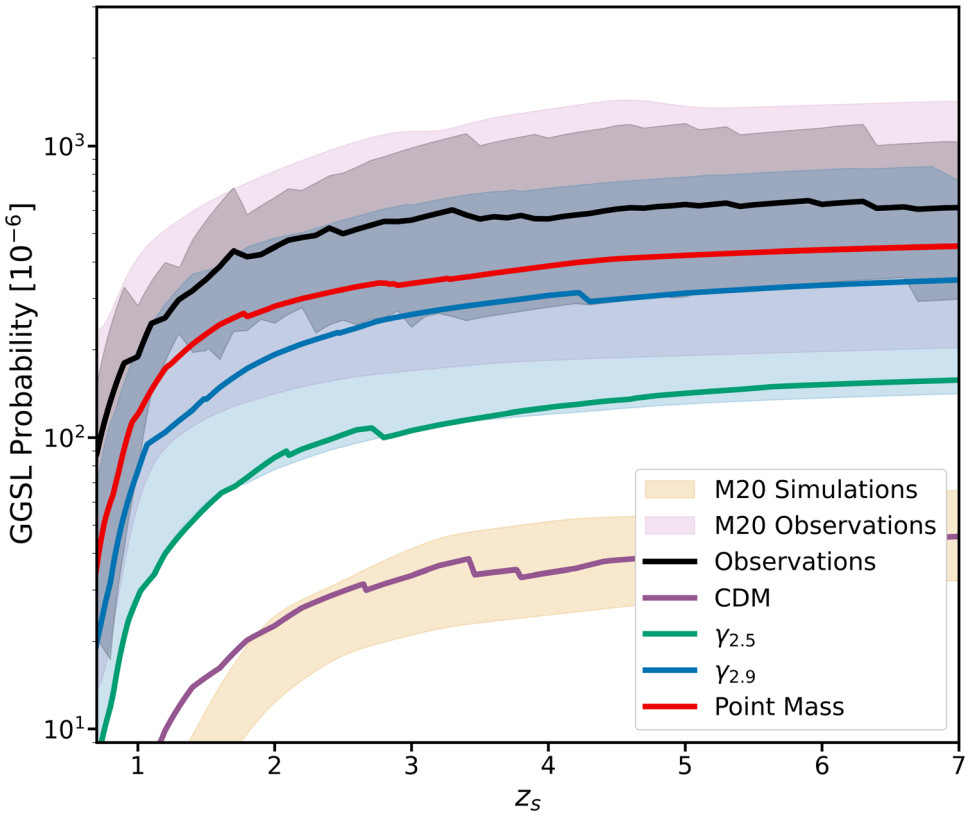

Figure 4. The GGSL probability as a function of source redshift for observed clusters, simulated mass-matched analogs in CDM, and c-SIDM. The mean GGSL probability of our sample is shown in black, and its range is depicted with a gray band. The median GGSL probability for the CDM TNG300 simulation suite is shown by a purple line, the blue and green lines show the median GGSL probability of the mimicked CDM subhalos undergoing core collapse, we show the 95th percentile with enhanced central density with the blue band, and the GGSL for the final collapsed subhalos in the limit as point masses is plotted with the red line. Pink and orange bands signify the range of GGSL probability for observed clusters and simulations, respectively, from M20.

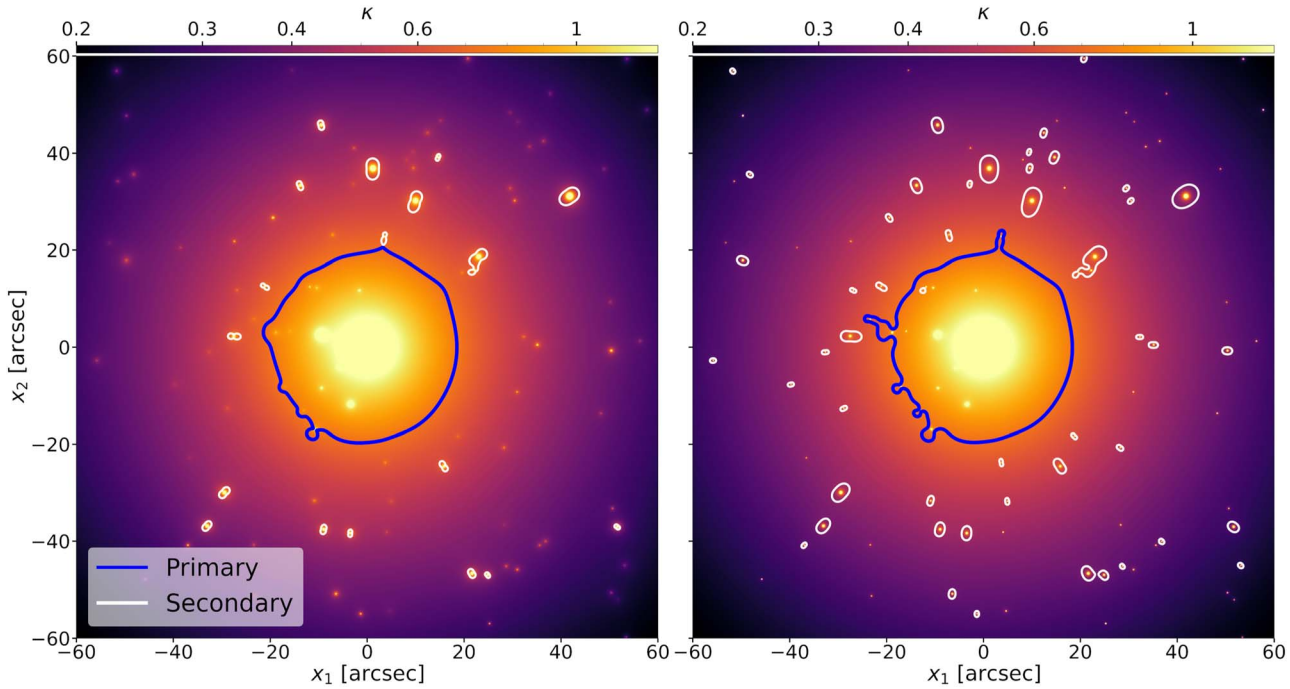

Figure 5. CDM and c-SIDM critical lines of a 10^{15} $M_\odot$ halo found in the TNG300 simulation. The left figure shows the critical lines of the halo modeled with CDM profiles, while the right shows the steeper γ profiles. The critical lines of these steepened subhalos increase in area and number as more subhalos become supercritical, while the subhalo critical lines close enough to the center merge with the primary critical line, creating visible distortions on its contours.

package instead of Lenstool, as done previously by M20. Our observed cluster sample has common candidates with the M20 sample but also includes a massive cluster, PG311, that has been selected not for its observed lensing properties but rather for the SZ decrement it produced as detected by the Planck satellite (Planck Collaboration et al. 2014). With this new methodology and use of an entirely independently generated Illustris simulation suite for comparison, the computed GGSL still remains discrepant by an order of magnitude, as reported previously. We also quantify the impact of projection effects and the inclusion of subhalo ellipticity on the computed GGSL for simulated subhalos and find no significant increase in the GGSL probability from either factor. Therefore, projection effects and the inclusion of ellipticity for cluster subhalos cannot bridge the order-of-magnitude GGSL discrepancy.

We now investigate how modifying the central density profile of cluster subhalos affects the GGSL cross section. We note that explicitly including the contribution of stars in the inner regions also alters CDM density profiles, but this effect results in $\gamma < 2.0$, insufficient to completely alleviate the GGSL discrepancy (F. M. Heinze et al. 2023; Y. M. Tokayer et al. 2024).

The modifications we make to rearrange the mass in the inner regions of simulated subhalo density profiles are intended to replicate the various stages of ongoing core collapse predicted by SIDM theories. We vary the inner logarithmic slopes γ in the profile shown in Equation (1), starting initially with the CDM NFW inner slope of 1 and steepening it to 3. Simulations of SIDM subhalos exhibit a variety of inner profile slopes that fall within this range (E. O. Nadler et al. 2023).

We find that the GGSL probability increases as the inner slope steepens, as noted by D. Yang & H.-B. Yu (2021). The median GGSL probability depends on the inner slope γ. When $\gamma = 1.5$, the GGSL probability is roughly 1.5 times higher than for CDM; for $\gamma = 2$, it increases to roughly 2 times that of CDM; for $\gamma = 2.5$, it is 3.5 times; and for the nearly ultimate stage of core collapse with $\gamma = 2.9$, it is found to increase by a factor of 8, bringing the GGSL cross section from simulations into agreement with what is found for observed cluster lenses. We draw attention to the fact that the radial distribution of cluster galaxies and their associated subhalos is not well reproduced in all CDM simulations including Illustris-TNG as demonstrated in P. Natarajan et al. (2017). Therefore, if this additional mismatch is attended to in simulations, it would result in the production of more massive subhalos closer to the cluster center, which would in turn also increase the GGSL. More accurately reproducing observed cluster galaxy properties within CDM is an ongoing challenge and project for all simulators, and this involves implementing more physical models for star formation, black hole growth, and feedback (A. Ragagnin et al. 2022).

We conclude that subhalos possessing internal density profiles given by Equation (11) and inner slopes $\gamma \sim 3$ can resolve the GGSL discrepancy. This enhancement of the GGSL probability occurs due to the large number of subhalos that become supercritical for lensing in cluster environments. The increased GGSL probability results from the steepened profile slope and the additional boost provided by the larger-scale mass components in the cluster (discussed further in Section 3). Note that NFW halos in field environments with $\gamma \sim 1$ are subcritical and cannot themselves generate multiple images. The supercritical densities on these scales in CDM come from the added contribution of baryonic matter. If one invokes a baryonic solution that increases the central density of a halo by rearranging stellar mass instead of dark matter, our results show that the required outcome must reproduce a mass density profile given by Equation (11) with $\gamma > 2.5$. However, no known mechanisms cause this level of steepening on the scales required to explain the GGSL discrepancy (F. M. Heinze et al. 2023).

The steepening of inner dark matter profiles via multiple physical processes has been explored previously, including the following: (i) accretion of dark matter onto central black holes, which achieves $\gamma \simeq 2.3$ (P. Gondolo & J. Silk 2000) on scales of <1 pc; (ii) formation of dark matter spikes around intermediate-mass black holes resulting in $\gamma \simeq 2.25$; and (iii) the adiabatic assembly of black holes resulting in dark matter mounds (G. Bertone et al. 2024). None of the above steepen NFW profiles on the scales of interest for GGSL. Examining the impact of baryons concentrated in the inner regions of dark matter halos on the inner density profiles, A. Di Cintio et al. (2014a, 2014b) derived a relation between the inner density slope and the stellar-to-halo mass ratio for simulated galaxies in the MUGS and MaGICC projects, finding a steepening of $\gamma < 1.5$. This is insufficient to bridge the GGSL discrepancy. M. Schaller et al. (2015a, 2015b) report steepening of the NFW to $\gamma < 2.0$ in the EAGLE suite of cosmological simulations, while F. M. Heinze et al. (2023) found a steepening to $\gamma = 2$ when fitting subhalos in the TNG50 simulation; once again, these slopes are insufficient to produce the enhancement needed in the GGSL probability. Á. Moliné et al (2017, 2023) have shown that the central concentration of cluster subhalos is enhanced by virtue of them residing in denser environments by a factor of 2–3 compared to the standard concentration used in the NFW profile in the ΛCDM model. We find that increasing the concentration by this factor of 2–3 still does not help alleviate the GGSL discrepancy. For details, see the discussion and plot in Appendix D.

8. Conclusions and Discussion

Our simulations quantify the central density profiles of dark matter halos required to reproduce the observed GGSL probability of observed cluster lenses. Our results show that the galaxies in dense cluster environments have higher central densities than those produced in large-scale cosmological simulations of these structures. If the discrepancy arises entirely from systematic issues present in the simulations, it must enter at a level that increases the central densities of halos by 4 orders of magnitude, as seen in Figure 3. Á. Moliné et al (2017) have shown that the central concentration of simulated cluster subhalos is enhanced by virtue of their being in denser environments by a factor of 2–3 compared to the standard concentration used in the NFW profile in the ΛCDM model. We find that increasing the concentration by this factor of 2–3 still does not help alleviate the GGSL discrepancy. And in more recent work, using even higher-resolution ΛCDM simulations, Á. Moliné et al (2023) find even larger enhancements that depend on the distance of the subhalo from the cluster center, which is still insufficient to fully account for the GGSL discrepancy. However, we caution that these analyses are derived from dark-matter-only simulations that do not include baryonic feedback processes that redistribute matter on the smallest scales.

Therefore, the discrepancy between measurements and simulations based on CDM illustrated by Figure 4 implies that current state-of-the-art cosmological simulations do not accurately predict the internal structure of dark matter halos on scales of 10^{10}–$10^{12}\,M_{\odot}\,h^{-1}$. This scenario implies that these simulations have missing physics associated with the galaxy formation and feedback mechanisms in clusters, or they could point to different properties of the dark matter than predicted by CDM.

The calculation of the GGSL itself does not depend on dark matter physics. However, one can interpret the implied properties of halos within the context of dark matter physics, and in particular SIDM, which predicts enhanced central densities for subhalos through core collapse. To date, this process has mainly been studied in less massive halos outside of galaxy clusters.

The process of core collapse depends on both the internal structure of a dark matter halo and the amplitude of the self-interaction cross section of a halo (e.g., D. Yang & H.-B. Yu 2022). As shown by M. Kaplinghat et al. (2016), halos with different masses probe the SIDM cross section at different relative velocities. For the cluster subhalos considered in this work, the relevant velocity scales are $\sim$50–100 km s^{-1}, and thus the GGSL within the context of SIDM requires a self-interaction cross section on these velocity scales high enough to drive core collapse.

A natural question in this context is whether a viable SIDM cross section exists that can drive core collapse on these scales without violating constraints from other observational probes. At velocities of $\sim$1000 km s^{-1}, stringent upper limits on the cross-section amplitude $\sigma \lesssim 1\,\mathrm{cm}^2\,\mathrm{g}^{-1}$ (A. H. G. Peter et al. 2013; L. Sagunski et al. 2021) preclude values high enough to cause core collapse in cluster subhalos within the age of the Universe. However, inelastic scattering cross sections can accelerate the onset of core collapse and possibly result in core collapse within the age of the Universe on these scales with an interaction cross section $\mathcal{O}(1\mathrm{cm}^2\mathrm{g}^{-1})$ (R. Essig et al. 2019; R. Huo et al. 2020; S. O'Neil et al. 2023).

Alternatively, velocity-dependent cross sections can increase the cross-section amplitude on the velocity scales of interest, especially if a mechanism specific to cluster environments accelerates the onset of core collapse relative to galactic environments. Velocity-dependent cross sections arise naturally in SIDM models in which a dark matter particle with mass m_{χ} interacts through a light force carrier m_{ϕ} (S. Tulin et al. 2013a; M. Vogelsberger et al. 2016; B. Colquhoun et al. 2021; D. Yang & H.-B. Yu 2022). At low speeds ($v \propto \frac{m_{\phi}}{m_{\chi}}$), these cross sections typically scale inversely with relative velocity to a power α that varies from close to 0 for certain models with a weak potential (i.e., those in the Born regime) to values of α in the range -1 to -4 in the semiclassical or classical scattering regimes (S. Tulin et al. 2013a; B. Colquhoun et al. 2021). In such models, an immediate consequence of an appreciable cross section on the scales of cluster subhalos is that the cross-section amplitude on lower-mass scales is enhanced by a factor of $\left(\frac{v}{100\,\mathrm{km\,s^{-1}}}\right)^{-\alpha}$, corresponding to a factor of 100–1000 increase on the scales of dwarf galaxies $v \sim$ 10–50 km s^{-1} and by an even larger factor on the scales probed by GGSL (D. Gilman et al. 2021, 2023; Q. Minor et al. 2021). Alternatively, a cross section with a pronounced resonance precisely at the velocity scales relevant for cluster subhalos (e.g., S. Tulin et al. 2013b; X. Chu et al. 2019; D. Gilman et al. 2023) could drive collapse in these structures without violating constraints from other scales, although one could argue that these solutions are disfavored because they require fine-tuning of the particle physics model.

To understand whether SIDM presents a viable resolution to the GGSL tension requires high-resolution hydrodynamical simulations of SIDM on galaxy cluster scales with sufficient resolution to resolve the central density profiles of cluster subhalos as they collapse. A. Ragagnin et al. (2024) recently simulated SIDM on cluster scales and reported a central density enhancement of $\sim$20% in cluster subhalos, but their simulations did not have sufficient resolution to study core collapse, and thus this phenomenon on cluster scales remains unexplored. However, if one assumes that the GGSL tension reported by M20 stems entirely from the internal properties of cluster subhalos, SIDM models offer a viable solution through core collapse. Whether an SIDM solution on the scales of cluster subhalos can evade stringent constraints from other astrophysical probes remains an open question.

Acknowledgments

The authors acknowledge useful discussions with Massimo Meneghetti, Guillaume Mahler, Mathilde Jauzac, Yarone Tokayer, Simon Birrer, Urmila Chadayammuri, and Elena Rasia. The authors are grateful to the anonymous referee for the constructive feedback. P.N. gratefully acknowledges funding from the Department of Energy grant DE-SC0017660. D.G. acknowledges support for this work provided by The Brinson Foundation through a Brinson Prize Fellowship grant.

Software: astropy (T. A. Collaboration et al. 2022), numpy (C. R. Harris et al. 2020), scikit-image (Van Der Walt 2014), lenstronomy (S. Birrer & A. Amara 2018; S. Birrer et al. 2021).

Appendix A
Impact of Projection Effects on GGSL

We investigate the impact of projection effects on GGSL from the simulated analogs and find it to be negligible. For a simulated analog in our sample, we compute the GGSL probability for each independent projection for both CDM and the steepened version (labeled as c2-SIDM) and show the results in Figure 6. The highest computed GGSL probability at redshift $z = 7$ differs from the lowest by less than 20% for CDM and by $\sim$26% for c2-SIDM, insufficient in and of itself to account on its own for the reported GGSL discrepancy. Therefore, projection effects cannot alleviate the GGSL discrepancy due exclusively to one of the projections, for some clusters align in the direction of elongation of the cluster. As noted in previous works, such as P. Natarajan et al. (2017), the lensing determined subhalo mass function for clusters is in very good agreement with the one computed from mass-matched simulated analogs, as shown in Figure 7.

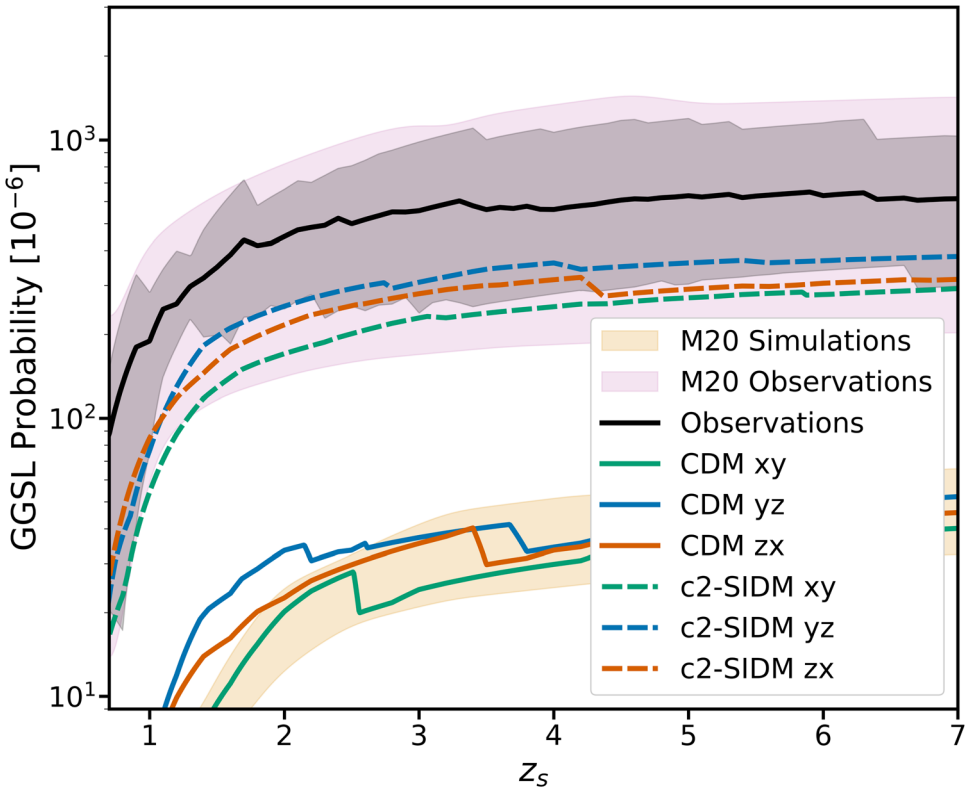

Figure 6. Impact of projection effects: change in GGSL probability as a function of source redshift along the three independent projections. Once again, the mean GGSL probability of our sample is shown in black and its range as a gray band. The GGSL probability for each independent projection for the selected CDM TNG300 analog is shown by solid lines in blue, green, and red; the dashed lines with corresponding colors show the GGSL probability of the steepened c2-SIDM.

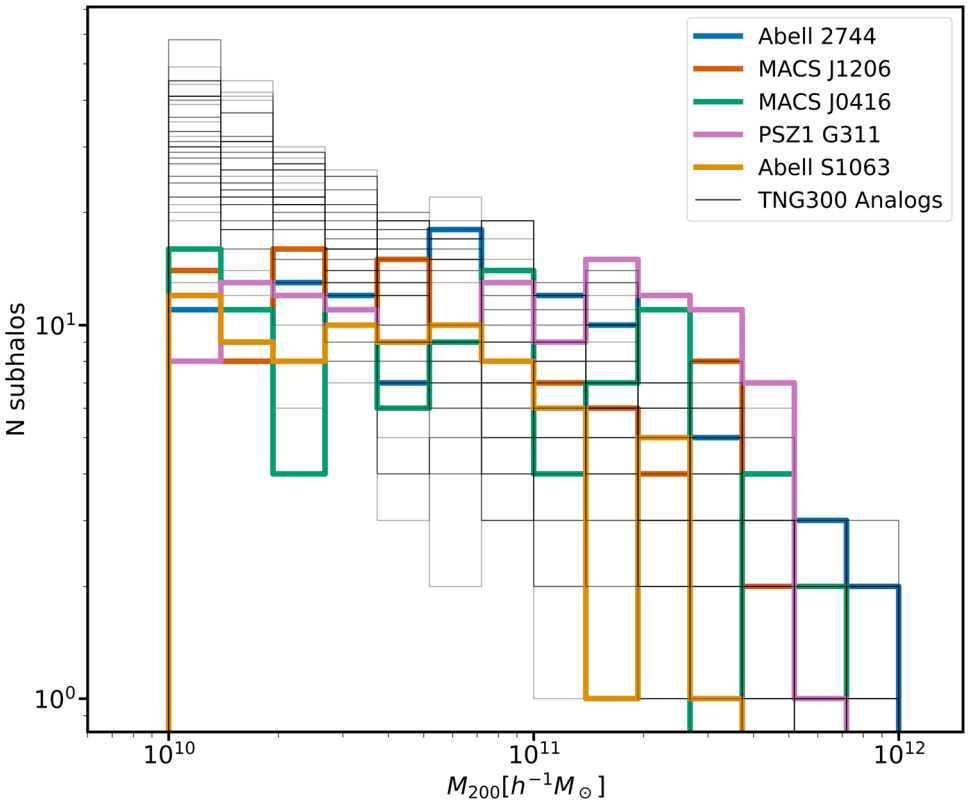

Figure 7. The subhalo mass function of observed clusters and their simulated CDM analogs in the TNG300 box. The solid colored lines are for the observed cluster sample, while gray lines show the subhalo mass distributions of the simulated CDM analogs.

Appendix B
Impact of Ellipticity on GGSL

We investigate the effect of subhalo ellipticity on our GGSL calculations and find that it is insufficient to fully account for the GGSL discrepancy. When computing the GGSL probability from simulations as described above, we first initialize a spherical NFW profile in `lenstronomy` for each subhalo in the mass-matched simulated cluster analog. We note that there are no observational constraints on the ellipticity of dark matter subhalos. Therefore, all the `Lenstool` parametric model files in our observed sample typically adopt spherically averaged profiles. However, if we assume that the ellipticity of the light distribution in an observed cluster member galaxy is a proxy for the ellipticity of its associated dark matter halo, as was done for the case of A2744, we can then construct an ellipticity distribution for the subhalo population. The `Lenstool` model for A2744 adopted this ellipticity distribution as a prior, and it is shown in the left panel of Figure 8.

The ellipticity $\hat{\epsilon}$ of a projected mass distribution with semimajor axis A and semiminor axis B is defined by

$$\hat{\epsilon} = \frac{A^2 - B^2}{A^2 + B^2}. \tag{B1}$$

Further details can be found in Á. Elìasdóttir et al. (2007, Appendix A.5 and references therein).

We adopt this observationally derived ellipticity distribution for subhalos in A2744 and draw uniformly from it to initialize elliptical NFW profiles in `lenstronomy` for each simulated analog and then compute the GGSL probability for the rest of our observed sample. The result can be seen in the left panel of Figure 8. We notice a slight increase in the GGSL probability by a factor of about 1.4 when the effects of subhalo ellipticity are included. However, the effect of ellipticity appears to be insignificant in and of itself to account for the observed GGSL discrepancy between simulations and observed cluster lenses.

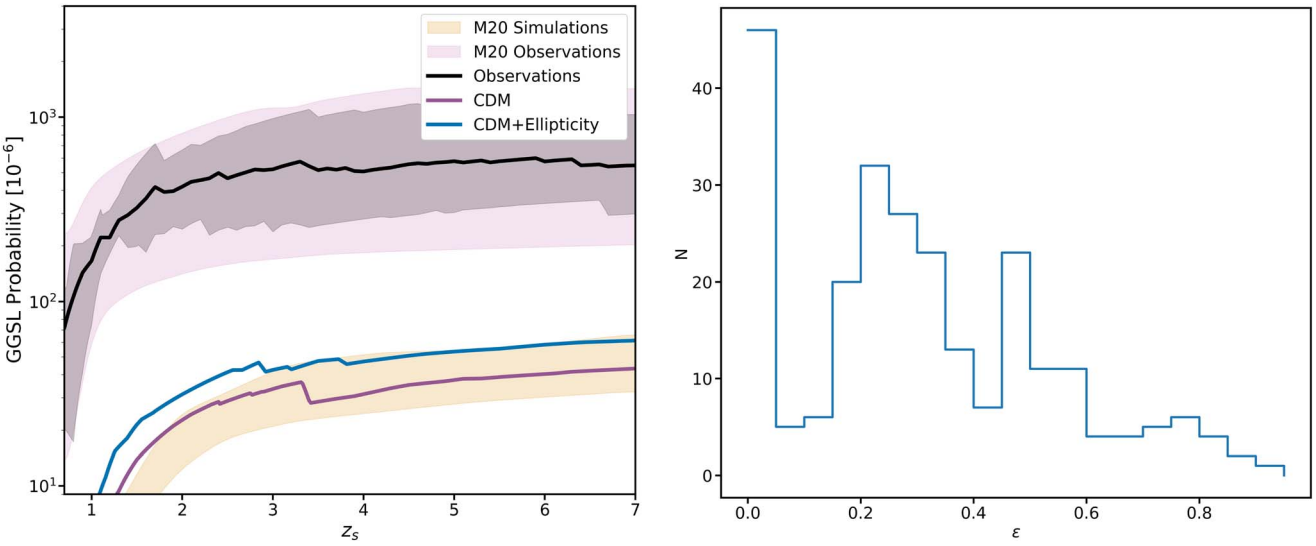

Figure 8. Left: comparison of the GGSL probability for spherical and elliptical subhalos. We compute the GGSL probability for the CDM TNG300 simulated analogs as spherical NFW profiles and overplot the calculation done with elliptical NFW profiles wherein the ellipticity is assigned to subhalos by drawing uniformly from A2744 ellipticity distribution.

Appendix C
Computing GGSL from Particle Data for Cluster Analogs in Illustris-TNG

We validate our NFW profile fits and the computation of the GGSL probability for mass-matched simulated analogs from the Illustris TNG300 simulation by computing the GGSL probability directly from the TNG300 particle data. To achieve this, we derive the deflection angle maps by tracing rays through the lens based on the projected mass distributions of these simulated halos, similar to the procedure employed in M20 and implemented in the publicly available code `Py-SPHViewer`.[14] We slice a box around the cluster with a depth of 20 Mpc and use a smoothed particle hydrodynamics scheme to create a convergence map, projecting each particle species separately (dark matter, gas, stars, and black holes) to achieve the final convergence map.

We compute the GGSL probability for the same mass-matched simulated analogs from TNG300 particle data for two distinct cases.

1. From the TNG300-1 simulation that includes dark matter and baryon particles, we compute the GGSL probability by creating a smoothed convergence map including only the dark matter particles in an effort to capture the effect of baryonic-induced adiabatic contraction on the dark matter halos.
2. From the TNG300-1 simulation that includes dark matter and baryon particles, we compute the GGSL probability by creating a smoothed convergence map including dark matter and baryon (gas, stars, and black holes) particles.

The resulting lensing critical lines and caustics of an observed cluster from our sample and a mass-matched simulated analog can be seen in Figure 9. We note that the Einstein radius, computed as specified in Section 3.2, of the primary critical line computed by fitting NFW profiles is 19″, while the one computed from the particle data is 18″. The results of GGSL probability computation are shown in Figure 2. We note that including the effects of baryon-driven contraction and all the baryonic components explicitly—namely, stars, gas, dust, and black holes—results in an enhancement of the GGSL probability; however, these are still insufficient to bridge the discrepancy with observations.

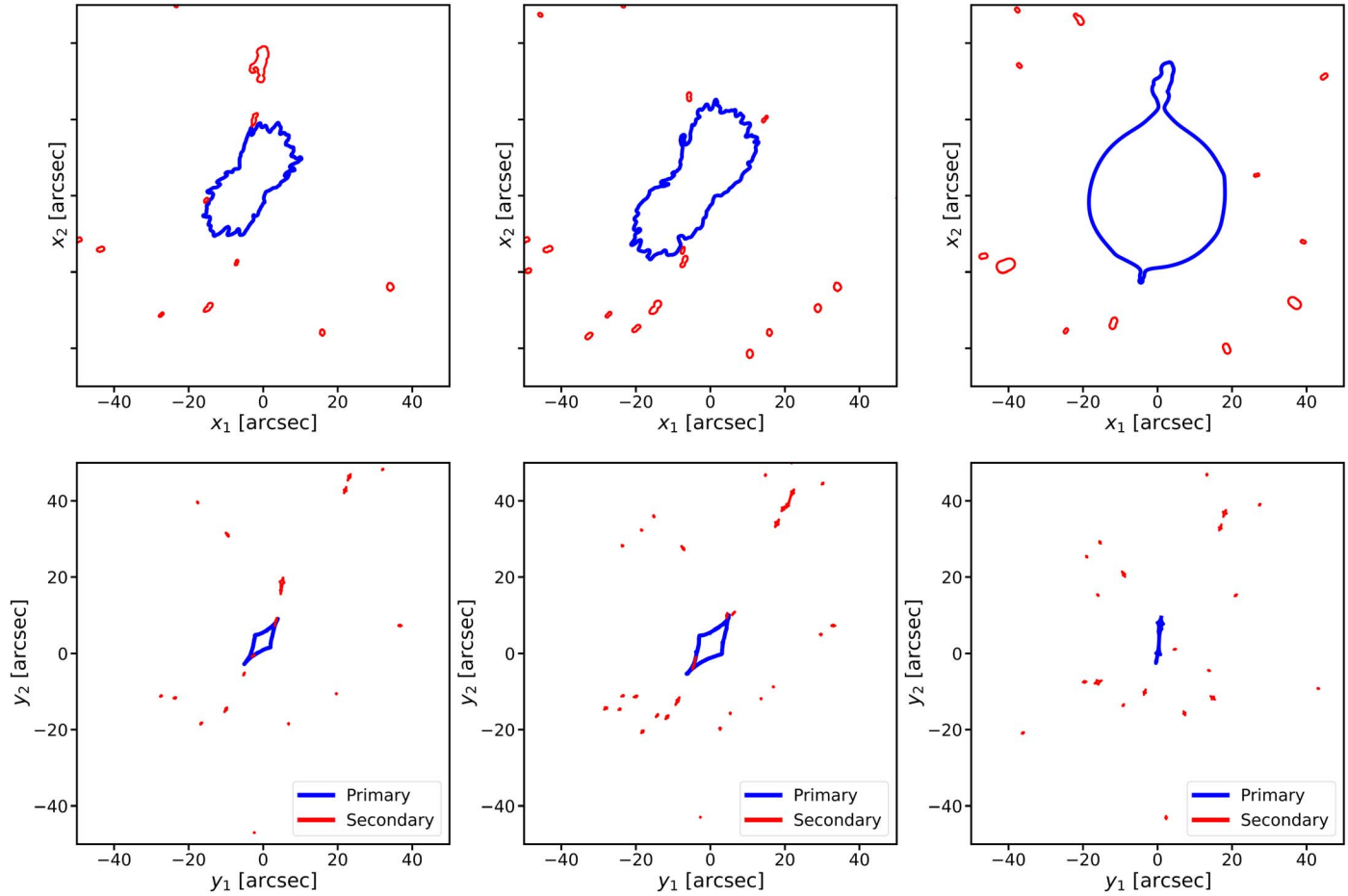

Figure 9. The lensing critical lines, shown in the top panels, and projected caustics, shown in the bottom panels, for the same TNG300 simulated analog. In the left panels and central panels of the figure, we plot the critical lines that were computed by smoothing and projecting the particle data as described above, only including dark matter particles (left panel) and including baryonic particles (central panel). The right panel shows the critical lines computed from our NFW fits.

[14] Publicly available at https://github.com/alejandrobll/py-sphviewer.

Appendix D
Impact of Subhalo Concentration on GGSL

While Y. M. Tokayer et al. (2024) found it insufficient to bridge the GGSL discrepancy, we investigate the impact of the NFW concentration parameter on the subhalo properties of interest, in this case, the GGSL probability.

As shown by Á. Moliné et al (2023) from the results of analyzing their high-resolution dark-matter-only Uchuu simulation, subhalos may be significantly more concentrated when residing inside massive hosts; specifically, those located in the inner regions have a significantly higher concentration than those in the outer regions. Using the Uchuu suite of dark-matter-only N-body cosmological simulations, Á. Moliné et al (2023) quantified subhalo concentrations using the parameter $c_{\rm v}$, defined as the mean density found at the radius of maximum circular velocity $R_{\rm V\,max}$, and found it to be in the range of 10^4–10^5 (for the subhalos considered here), decreasing for more massive subhalos. We note that the more familiar NFW concentration can be directly related to $c_{\rm v}$ (Á. Moliné et al 2017), including a dependence on the projected distance from the cluster center, via

$$c_{\rm v} = \left(\frac{c_{\rm NFW}}{2.163}\right)^3 \frac{f(R_{\rm max}/r_{\rm s})}{f(c_{\rm NFW})}\Delta, \tag{D1}$$

where $f(x) = \ln(1+x) - x/(1+x)$. The concentrations that we obtain for simulated subhalos are also higher than for comparable-mass isolated halos, and these tend to be outliers in the concentration–mass (c–M) relation in ΛCDM. However, as we have seen, this still does not translate into a high enough value for the GGSL probability to account for the discrepancy as shown above with halo catalogs and also with the particle data. As shown by Á. Moliné et al (2017) from the results of analyzing their high-resolution dark-matter-only Uchuu simulation, subhalos may be significantly more concentrated when residing inside massive hosts; specifically, those located in the inner regions have a significantly higher concentration than those in the outer regions, enhanced by up to a factor of ∼3 for less massive subhalos and ∼1.5 for more massive subhalos. We note that these enhancement factors are still insufficient to account for the GGSL probability in observed lensing clusters as shown in Figure 10.

As shown in Figure 3, we need a concentration of mass well inside the NFW scale radius (r_s) on scales less than $0.01 \times R_{200}$ to impact the GGSL probability and increase it significantly. We calculate $c_{\rm v}$, and subsequently $c_{\rm NFW}$, for all subhalos in our simulated analogs by following the parameterization given in Á. Moliné et al (2023):

$$c_{\rm v}(V_{\rm max}, x_{\rm sub}) = c_0\left[1 + \sum_{i=1}^{3}\left[a_i \log_{10}\left(\frac{V_{\rm max}}{\rm km\ s^{-1}}\right)\right]^i\right] \times [1 + b\log_{10}(x_{\rm sub})], \tag{D2}$$

where $x_{\rm sub} = r_{\rm sub}/R_{\rm vir,h}$ is the ratio of subhalo distance to the host halo center; $c_0 = 1.12 \times 10^5$; $a_i = -0.9512, -0.5538, -0.3221$; and $b = -1.7828$.

In the left panel of Figure 11, we show the values of c_v obtained for the mass-matched simulated analog Illustris subhalos given their $c_{\rm NFW}$. It is clearly seen to be very similar to the distribution derived by Á. Moliné et al (2023) in Figure 6 of their paper. In the right and middle panels, we show the

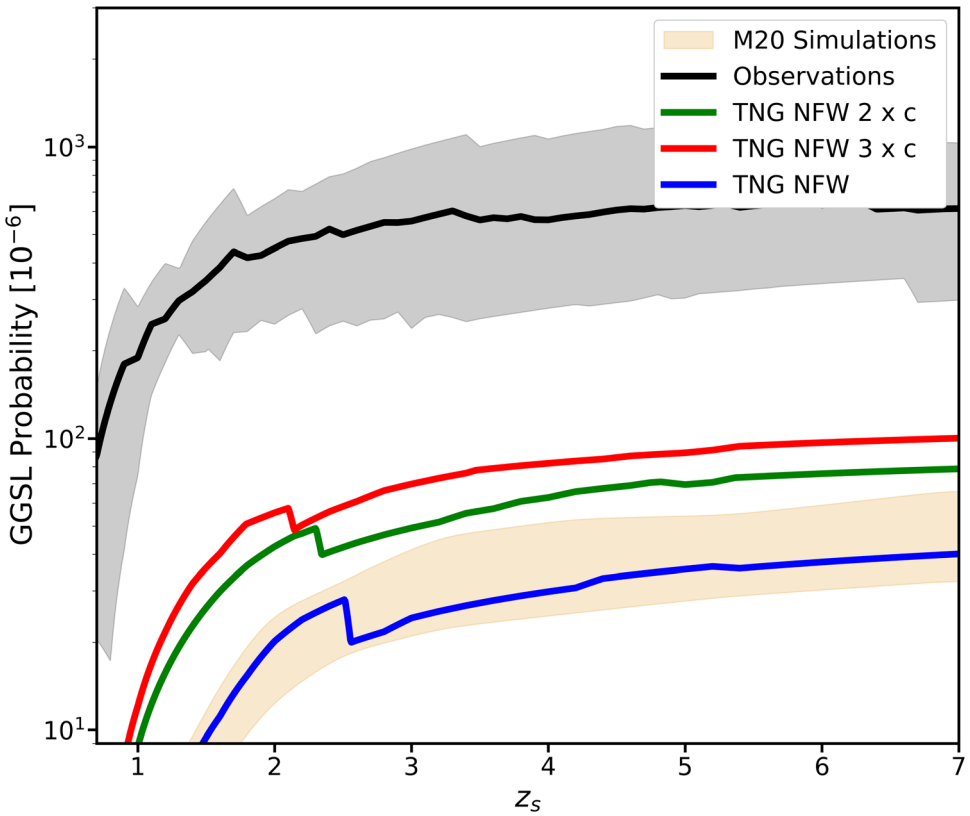

Figure 10. The GGSL probability computed for our simulated mass-matched Illustris subhalos including an enhancement in the NFW concentration parameter by factors of 2–3, as initially reported in Á. Moliné et al (2017). This increase does not alleviate the GGSL discrepancy.

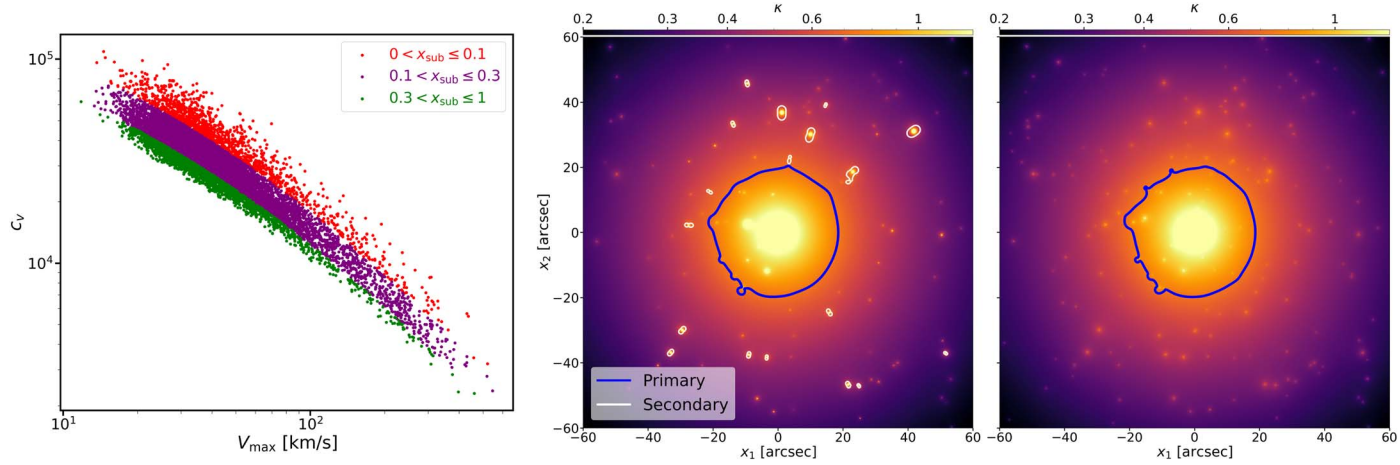

Figure 11. Left: the values of c_v computed from the c_{NFW} for our Illustris subhalos as a function of v_{max} using the conversion equation that includes the dependence on projected distance from the cluster center explicitly. We note that these distributions match those obtained by Á. Moliné et al (2023) in Figure 6 of their paper. Therefore, the claimed enhancement in concentration from their higher-resolution simulation Uchuu is also seen in Illustris-TNG300 subhalos. Middle and right: the convergence map of a simulated analog in TNG contrasting the critical lines obtained fitting subhalos with a concentration parameter used in this work (middle) to the ones obtained using the Á. Moliné et al (2023) concentration parameterization (right).

critical lines of a TNG simulated analog obtained from fitting the subhalo concentration parameter using the parameterization provided in Á. Moliné et al (2023) and contrast it to the critical lines obtained from the concentration adopted in this work, respectively. Therefore, our Illustris subhalos are as over-concentrated as the subhalos in their Uchuu simulation. However, as we have already shown in this work, the Illustris mass-matched analog subhalos fail to account for the GGSL discrepancy while using both the halo catalogs and the particle data directly. Redefining the concentration parameter does not alter their contribution to GGSL.

Therefore, we demonstrate that neither projection effects, ellipticity, nor concentration can fully alleviate the GGSL discrepancy.

ORCID iDs

Isaque Dutra https://orcid.org/0000-0001-7040-4930
Priyamvada Natarajan https://orcid.org/0000-0002-5554-8896
Daniel Gilman https://orcid.org/0000-0002-5116-7287

References

Astropy Collaboration, Price-Whelan, A. M., Lim, P. L., et al. 2022, ApJ, 935, 167
Babyk, I., Elyiv, A., Melnyk, O., & Krivodubskij, V. N. 2012, KPCB, 28, 69
Bahé, Y. M. 2021, MNRAS, 505, 1458
Balberg, S., Shapiro, S. L., & Inagaki, S. 2002, ApJ, 568, 475
Balestra, I., Mercurio, A., Sartoris, B., et al. 2016, ApJS, 224, 33
Bartelmann, M., Huss, A., Colberg, J. M., Jenkins, A., & Pearce, F. R. 1998, A&A, 330, 1
Bergamini, P., Rosati, P., Mercurio, A., et al. 2019, A&A, 631, A130
Bergamini, P., Rosati, P., Vanzella, E., et al. 2021, A&A, 645, A140
Bertone, G., Wierda, A. R. A. C., Gaggero, D., et al. 2024, arXiv:2404.08731
Bezanson, R., Labbe, I., Whitaker, K. E., et al. 2024, ApJ, 974, 92
Birrer, S., & Amara, A. 2018, PDU, 22, 189
Birrer, S., Shajib, A., Gilman, D., et al. 2021, JOSS, 6, 3283
Biviano, A., Rosati, P., Balestra, I., et al. 2013, A&A, 558, A1
Bonamigo, M., Grillo, C., Ettori, S., et al. 2017, ApJ, 842, 132
Bradač, M., Lombardi, M., & Schneider, P. 2004, A&A, 424, 13
Bullock, J. S., & Boylan-Kolchin, M. 2017, ARA&A, 55, 343
Caminha, G. B., Grillo, C., Rosati, P., et al. 2016, A&A, 587, A80
Chu, X., Garcia-Cely, C., & Murayama, H. 2019, PhRvL, 122, 071103
Colquhoun, B., Heeba, S., Kahlhoefer, F., Sagunski, L., & Tulin, S. 2021, PhRvD, 103, 035006
Dahle, H., Aghanim, N., Guennou, L., et al. 2016, A&A, 590, L4
Di Cintio, A., Brook, C. B., Dutton, A. A., et al. 2014a, MNRAS, 441, 2986
Di Cintio, A., Brook, C. B., Macciò, A. V., et al. 2014b, MNRAS, 437, 415
Diego, J. M., Broadhurst, T., Wong, J., et al. 2016, MNRAS, 459, 3447
Ebeling, H., Ma, C. J., Kneib, J.-P., et al. 2009, MNRAS, 395, 1213
Elìasdóttir, Á., Limousin, M., Richard, J., et al. 2007, arXiv:0710.5636
Essig, R., McDermott, S. D., Yu, H.-B., & Zhong, Y.-M. 2019, PhRvL, 123, 121102
Fischer, M. S., Dolag, K., & Yu, H.-B. 2024, A&A, 689, A300
Gilman, D., Bovy, J., Treu, T., et al. 2021, MNRAS, 507, 2432
Gilman, D., Zhong, Y.-M., & Bovy, J. 2023, PhRvD, 107, 103008
Gómez, P. L., Valkonen, L. E., Romer, A. K., et al. 2012, AJ, 144, 79
Gondolo, P., & Silk, J. 2000, NuPhS, 87, 87
Grillo, C., Suyu, S. H., Rosati, P., et al. 2015, ApJ, 800, 38
Gruen, D., Brimioulle, F., Seitz, S., et al. 2013, MNRAS, 432, 1455
Harris, C. R., Millman, K. J., Van Der Walt, S. J., et al. 2020, Natur, 585, 357
Heinze, F. M., Despali, G., & Klessen, R. S. 2023, MNRAS, 527, 11996
Huo, R., Yu, H.-B., & Zhong, Y.-M. 2020, JCAP, 2020, 051
Jauzac, M., Clément, B., Limousin, M., et al. 2014, MNRAS, 443, 1549
Jauzac, M., Eckert, D., Schwinn, J., et al. 2016, MNRAS, 463, 3876
Jauzac, M., Richard, J., Jullo, E., et al. 2015, MNRAS, 452, 1437
Kaplinghat, M., Tulin, S., & Yu, H.-B. 2016, PhRvL, 116, 041302
Kneib, J.-P., & Natarajan, P. 2011, A&ARv, 19, 47
Lotz, J. M., Koekemoer, A., Coe, D., et al. 2017, ApJ, 837, 97
Lynden-Bell, D., Wood, R., & Royal, A. 1968, MNRAS, 138, 495
Mace, C., Zeng, Z. C., Peter, A. H. G., et al. 2024, arXiv:2402.01604
Mahler, G., Richard, J., Clément, B., et al. 2018, MNRAS, 473, 663
Meneghetti, M., Cui, W., Rasia, E., et al. 2023, A&A, 678, L2
Meneghetti, M., Davoli, G., Bergamini, P., et al. 2020, Sci, 369, 1347
Meneghetti, M., Ragagnin, A., Borgani, S., et al. 2022, A&A, 668, A188
Merten, J., Coe, D., Dupke, R., et al. 2011, MNRAS, 417, 333
Minor, Q., Gad-Nasr, S., Kaplinghat, M., & Vegetti, S. 2021, MNRAS, 507, 1662
Mo, H., van den Bosch, F. C., & White, S. 2010, Galaxy Formation and Evolution (Cambridge: Cambridge Univ. Press),
Moliné, Á., Sánchez-Conde, M. A., Aguirre-Santaella, A., et al. 2023, MNRAS, 518, 157
Moliné, Á., Sánchez-Conde, M. A., Palomares-Ruiz, S., & Prada, F. 2017, MNRAS, 466, 4974
Munari, E., Grillo, C., Lucia, G. D., et al. 2016, ApJL, 827, L5
Munoz, J. A., Kochanek, C. S., & Keeton, C. R. 2001, ApJ, 558, 657
Nadler, E. O., Yang, D., & Yu, H.-B. 2023, ApJL, 958, L39
Natarajan, P., Chadayammuri, U., Jauzac, M., et al. 2017, MNRAS, 468, 1962
Natarajan, P., & Kneib, J.-P. 1997, MNRAS, 287, 833
Natarajan, P., Williams, L. L. R., Bradač, M., et al. 2024, SSRv, 220, 19
Navarro, J. F., Frenk, C. S., & White, S. D. M. 1997, ApJ, 490, 493
Nelson, D., Springel, V., Pillepich, A., et al. 2019, ComAC, 6, 2
O'Neil, S., Vogelsberger, M., Heeba, S., et al. 2023, MNRAS, 524, 288
Peter, A. H. G., Rocha, M., Bullock, J. S., & Kaplinghat, M. 2013, MNRAS, 430, 105

Planck Collaboration, Ade, P. A. R., Aghanim, N., et al. 2014, A&A, 571, A29
Planck Collaboration, Aghanim, N., Akrami, Y., et al. 2020, A&A, 641, A6
Postman, M., Coe, D., Benìtez, N., et al. 2012, ApJS, 199, 25
Ragagnin, A., Meneghetti, M., Bassini, L., et al. 2022, A&A, 665, A16
Ragagnin, A., Meneghetti, M., Calura, F., et al. 2024, A&A, 687, A270
Rexroth, M., Natarajan, P., & Kneib, J.-P. 2016, MNRAS, 460, 2505
Rivera-Thorsen, T. E., Dahle, H., Gronke, M., et al. 2017, A&A, 608, L4
Robertson, A. 2021, MNRAS: Letters, 504, L7
Sagunski, L., Gad-Nasr, S., Colquhoun, B., Robertson, A., & Tulin, S. 2021, JCAP, 2021, 024
Sales, L. V., Wetzel, A., & Fattahi, A. 2022, NatAs, 6, 897
Schaller, M., Frenk, C. S., Bower, R. G., et al. 2015a, MNRAS, 451, 1247
Schaller, M., Frenk, C. S., Bower, R. G., et al. 2015b, MNRAS, 451, 343
Sharon, K., Mahler, G., Rivera-Thorsen, T. E., et al. 2022, ApJ, 941, 203
Slone, O., Jiang, F., Lisanti, M., & Kaplinghat, M. 2023, PhRvD, 107, 043014
Spergel, D. N., Bean, R., Dore, O., et al. 2007, ApJS, 170, 377
Spergel, D. N., & Steinhardt, P. J. 2000, PhRvL, 84, 3760
Tokayer, Y. M., Dutra, I., Natarajan, P., et al. 2024, ApJ, 970, 143
Tulin, S., Yu, H.-B., & Zurek, K. M. 2013a, PhRvL, 110, 111301
Tulin, S., Yu, H.-B., & Zurek, K. M. 2013b, PhRvD, 87, 115007
Umetsu, K., Medezinski, E., Nonino, M., et al. 2012, ApJ, 755, 56
Umetsu, K., Zitrin, A., Gruen, D., et al. 2016, ApJ, 821, 116
van den Bosch, F. C., Ogiya, G., Hahn, O., & Burkert, A. 2018, MNRAS, 474, 3043
Van Der Walt, S., Schönberger, J. L., Nunez-Iglesias, J., et al. 2014, PeerJ, 2, e453
Vogelsberger, M., Zavala, J., Cyr-Racine, F.-Y., et al. 2016, MNRAS, 460, 1399
Williamson, R., Benson, B. A., High, F. W., et al. 2011, ApJ, 738, 139
Yang, D., & Yu, H.-B. 2021, PhRvD, 104, 103031
Yang, D., & Yu, H.-B. 2022, JCAP, 2022, 077
Yang, S., Du, X., Zeng, Z. C., et al. 2023, ApJ, 946, 47
Zavala, J., Lovell, M. R., Vogelsberger, M., & Burger, J. D. 2019, PhRvD, 100, 063007
Zeng, Z. C., Peter, A. H. G., Du, X., et al. 2022, MNRAS, 513, 4845